Multicomponent Spray Computations in a Modified Centerbody Combustor

M. S. Raju* and W. A. Sirignano†
University of California, Irvine, Irvine, California

The flow properties of the near-wake region of a ducted, bluff-body combustor are presented, based upon finite-difference computations involving turbulent, reacting flows with polydisperse and multicomponent sprays. The analysis advances the state-of-the-art for the representation of the liquid-phase and for the coupling between the phases. The gas phase representation is existing state-of-the-art. Both droplet vaporization and turbulent mixing rates are found to be rate-controlling in the primary reaction region, and the mixing rate is identified to be the rate-controlling process in the later stages of combustion. Under the inflow conditions leading to an equivalence ratio of one based on the primary air/fuel mass flow rates, the primary reaction region is found to be fuel-rich. Enhanced energy conversion is observed to result from improved mixing; the effects of fuel composition are found to be negligible. Near the wake-extinction limit of the combustor the effects of fuel composition are found to be very significant.

Nomenclature

a = exponents of fuel mole fraction in Eq. (2)
b = exponent of oxidizer mole fraction in Eq. (2)
A' = $A(W'_c/\rho'_c)^{a+b-1}t'_c$, pre-exponential coefficient in Eq. (2)
b_1 = $120/T'_c$, constant in Eq. (29)
B_k = the Spalding transfer number in Eq. (19)
C_D = droplet drag coefficient in Eq. (12)
$C(t)$ = droplet regression rate in Eq. (14)
C'_p = $C_pC_{p,c}$, specific heat, J/kg K
C_p = nondimensional specific heat
$C'_{p,c}$ = specific heat of gas at inflow, J/kg K
D' = binary diffusion coefficient, m^2/s
dV'_ϕ = $dV_\phi r'^3_c$, the computational cell volume for the variable ϕ, m^3
dV_ϕ = nondimensional cell volume
E'_i = $E_{ai}R'T'_c$, activation energy, J/mol
E_{ai} = nondimensional activation energy
f = Emmons' form of Blasius function
g'_i = square of the concentration fluctuations
h' = $hC'_{p,c}T'_c$, enthalpy, J/kg
h = nondimensional enthalpy
k' = kU'^2_c, kinetic energy of turbulence, m^2/s^2
ℓ'_i = $\ell_iC'_{p,c}T'_c$, heat of vaporization of ith species, J/kg
ℓc_i = appears in Eq. (23), $\ell'_i/R'T'_c/W'_{fi}$
ℓ_k = latent heat of vaporization of multicomponent mixture
L_K = $r'_c/r'_{k,o}$, ratio of characteristic length to the initial drop size
m'_k = $m_k\mu'_cr'_{k,o}$, droplet vaporization rate, kg/s
m_k = nondimensional droplet vaporization rate
M_c = $U'_c/(\nu_cR'_cT'_c)^{1/2}$, characteristic Mach number
n_k = the number of droplets in kth Lagrangian characteristic
P' = $P\rho'_cU'^2_c$, gas pressure, Pa
P = nondimensional gas pressure
P'_{is} = $P_{is}\rho'_cU'^2_c$, partial pressure of ith species at droplet surface, Pa
Pe_ℓ = liquid phase Peclet number, $Re_\ell Pr_\ell$
Pr_c = gas phase Prandtl number, $\mu'_cC'_{p,c}/k'_c$
Pr_ℓ = liquid phase Prandtl number, $\mu'_\ell C'_{p,\ell}/k'_\ell$
Q'_i = $QC'_{p,c}T'_c$, heat of reaction, J/kg
Q = nondimensional heat of reaction
r'_c = the characteristic length, m
r'_k = $r_kr'_{k,0}$, droplet radius, m
r_k = nondimensional droplet radius
$r'_{k,0}$ = the initial droplet radius, m
R' = universal gas constant, J/mol K
R_{fi} = reaction rate defined in Eq. (2)
Re_c = gas phase Reynolds number, $U'_cr'_c\rho'_c/\mu'_c$
Re_ℓ = liquid phase Reynolds number, $U'_cr'_{k,0}\rho'_\ell/\mu'_\ell$
Re_k = droplet Reynolds number defined in Eq. (11)
S_k = $r'^2_k/r'^2_{k,0}$, radius squared
$S_{\phi,g}$ = the source terms appearing in Eq. (1)
$S_{\phi,\ell}$ = the additional source terms of Eq. (1) arising from the liquid- to gas-phase interaction
Sc_c = gas phase Schmidt number, $\mu'_c/\rho'_cD'_c$
Sc_ℓ = liquid phase Schmidt number, $\mu'_\ell/\rho'_\ell D'_\ell$
t' = tt'_c, time, s
t = nondimensional time
t'_c = r'_c/U'_c, the characteristic time, s
T' = TT'_c, gas temperature, K
T = nondimensional temperature
T'_b = $T_bT'_c$, liquid boiling temperature at normal pressure, K
T_b = nondimensional boiling temperature
T'_c = characteristic temperature, K
T'_k = $T_kT'_c$, droplet surface temperature, K
T_k = nondimensional droplet surface temperature
U' = UU'_c, gas velocity in the axial direction, m/s
U = nondimensional axial gas velocity
U'_c = characteristic velocity, m/s
U'_k = $U_kU'_c$, axial component of droplet velocity, m/s
U_k = nondimensional axial component of droplet velocity
V' = VU'_c, gas velocity in the radial direction, m/s
V = nondimensional radial gas velocity
V'_k = $V_kU'_c$, radial component of droplet velocity, m/s
V_k = nondimensional radial component of droplet velocity
W' = WU'_c, gas velocity in the tangential direction, m/s
W = nondimensional tangential gas velocity
W'_a = $W_aW'_c$, molecular weight of the mixture, excluding fuel vapor, kg/mol

Received Feb. 18, 1988; revision received June 7, 1989.

*Department of Mechanical Engineering; currently, Senior Engineer at Sverdrup Tech., Inc., Cleveland, OH.
†Professor, Department of Mechanical Engineering. Fellow AIAA.

W_a = nondimensional mixture molecular weight without fuel vapor
W_c' = molecular weight of the air, kg/mol
W_i' = $W_i W_c'$, molecular weight of ith species, kg/mol
W_i = nondimensional molecular weight of ith species
W_k = nondimensional tangential component of droplet velocity
W_k' = $W_k U_c'$ tangential component of droplet velocity, m/s
x' = $x r_c'$, axial distance, m
x = nondimensional axial distance
y' = $y r_c'$, radial distance, m
y = nondimensional radial distance
Y_i = mass fraction of the species
Γ_ϕ' = $\Gamma_\phi \mu_c'$, exchange coefficient in Table 1, kg/s/m
Γ_ϕ = nondimensional exchange coefficient
δ_i = fractional mass evaporation rate of fuel species
ϵ' = $\epsilon U_c'^2 / t_c'$, dissipation rate of energy, m^2/s^3
ϵ = nondimensional dissipation rate
η = represents the streamline of a Hill's vortex in the circulating fluid in Eqs. (14–18)
θ = half-angle of the element of cone spray, °
μ' = $\mu \mu_c'$, viscosity, Pa·s
μ = nondimensional viscosity
μ_c' = viscosity of air at inflow, Pa·s
ν = stoichiometric ratio
ν_c = ratio of the specific heats
ρ' = $\rho \rho_c'$, density, kg/m^3
ρ = nondimensional density
ρ_c' = density of air at inflow, kg/m^3
σ_ϕ = represents Sc_c or Pr_c for variable ϕ
ϕ = represents dependent variable of Eq. (1)
Φ = equivalence ratio
χ_i = mole fraction of ith species

Subscripts

a = air
b = boiling
c = characteristic conditions
eff = effective
f = fuel
g = gas-phase
i = species
k = droplet or Lagrangian characteristics representing a group of particles
ℓa = laminar
ℓ = liquid phase
n = normal conditions
o = oxidizer
s = droplet surface
t = turbulent
w = wall
O = liquid-phase initial conditions

I. Introduction

THE objective of the present study is to develop a detailed solution procedure via finite-difference calculations for the prediction of the flow properties in recirculating, continuous spray combustors such as those encountered in gas-turbines, hazardous waste incinerators, and furnaces. The mathematical formulation involves simultaneous consideration of fuel evaporation, turbulent mixing, chemical kinetics, and multidimensional fluid mechanics. Over the last decade, considerable effort has gone into the development of numerical procedures to predict the combustor performance involving single-component liquid sprays, e.g., El Banhawy and Whitelaw,[1] Swithenbank et al.,[2] and Raju and Sirignano,[3] among many others. One important aspect of spray combustion that has not received much attention is the multicomponent nature of the liquid sprays. The conventional petroleum based liquid fuels utilized in gas-turbine combustors comprise mixtures of many compounds, and thus exhibit a wide range of physical and chemical properties.[4] Recently, there has been considerable interest in the area of hazardous waste incinerators, where waste is mixed with the conventional fuels to promote the ignition and combustion characteristics of the hazardous compounds.[5] The importance of multicomponent spray modeling becomes more evident because of the increasing need for considering jet fuels derived from heavier petroleum fractions.[6] The ignition characteristics, blow-off conditions and extinction limits of the combustor could also be influenced by nonuniform concentration of the fuels of different volatilities. Although various vaporization models have been developed to account for the effects associated with the multicomponent nature of the fuel, none of the earlier studies have considered the multicomponent fuels in a comprehensive modeling treatment of the practical combustor systems.

In the present study, the unsteady, two-dimensional, gas-phase equations describing motion and transport are represented in Eulerian coordinates, and the liquid-phase equations are represented in Lagrangian coordinates. For the multicomponent sprays, it is important to consider the transient nature of the liquid-phase mass transport. Liquid mass diffusion is very slow compared to heat diffusion (or the droplet regression rate), as the Schmidt number (or the Peclet number based on regression rate and mass diffusivity) of a typical hydrocarbon liquid fuel in a high-temperature gas is around one hundred.[7] The transient droplet heating also remains important during most of the droplet lifetime, as the liquid-phase Prandtl number is typically of the order of ten. Therefore, it is important to choose a vaporization model that takes into account the details of transient thermal and mass transport, together with the fluid mechanics of the droplet interior and of the surrounding gas film, since they effect the droplet vaporization characteristics. In the present study, the liquid-phase phenomena are modeled by the simplified vortex model of Tong and Sirignano.[8] During the earlier portion of the droplet lifetime, the droplet vaporization rate is determined based on the simplified gas-phase boundary-layer analysis of Tong and Sirignano,[8] which is valid for droplet Reynolds numbers of 0(100). However, during the final stages of the droplet lifetime, it is necessary to switch to a valid low Reynolds number model, as the droplet Reynolds number becomes very low; the low Reynolds number model chosen is based on a correlation obtained from Clift et al.[9] The turbulent phenomena are described by the k-ϵ model of Launder and Spalding,[10] and the combustion phenomena are described by the model developed by Khalil et al.[11] The governing equations are solved by the numerical procedure outlined in Raju and Sirignano,[3] which is modified to include the additional features of the flow configuration, such as multicomponent sprays and swirl flows.

The numerical procedure is applied to simulate the near-wake region of a ducted bluff-body configuration, which involves the interaction between one or two annular air streams and a liquid spray. A limited parametric study is undertaken to identify the influence of swirl number, fuel composition, the ratio of fuel/air mass flow rates, and the addition of a separate dilution stream on the vaporization, mixing, and combustion characteristics of the primary and secondary reaction regions.

II. Gas-Phase Equations

The governing equations based on the conservation of the gas-phase flow properties for confined subsonic recirculating flows are, in general, elliptic in space and parabolic in time. For axisymmetric geometries, the gas-phase equations in Eulerian coordinates can be expressed by the following form:

$$\frac{\partial \rho\phi}{\partial t} + \frac{\partial}{\partial x}\left[\rho U\phi - \Gamma_\phi \frac{\partial \phi}{\partial x}\right] + \frac{1}{y}\frac{\partial}{\partial y}\left[y\rho V\phi - y\Gamma_\phi \frac{\partial \phi}{\partial y}\right] = S_{\phi,g} + S_{\phi,\ell} \quad (1)$$

Table 1 Source terms appearing in Eq. (1)

Equation	ϕ	Γ_ϕ	$S_{\phi,g}$	$dV_\phi S_{\phi,\ell} = s_{\phi,\ell}$
Continuity	1	0	0	$\frac{1}{Re_c}\sum\frac{1}{L_k}n_k m_k$
Axial momentum	U	μ_{eff}	$-\frac{\partial P}{\partial x}+\frac{\partial}{\partial x}\left(\Gamma_\phi\frac{\partial U}{\partial x}\right)+\frac{1}{y}\frac{\partial}{\partial y}\left(y\Gamma_\phi\frac{\partial V}{\partial x}\right)$	$\frac{1}{Re_c}\sum\frac{1}{L_k}\left(n_k m_k U_k-\frac{4\pi}{3}\rho_k r_k^3 n_k F_{\phi,k}\right)$
Radial momentum	V	μ_{eff}	$-\frac{\partial P}{\partial y}-\frac{2\Gamma_\phi V}{y^2}+\frac{\partial}{\partial x}\left(\Gamma_\phi\frac{\partial U}{\partial y}\right)+\frac{1}{y}\frac{\partial}{\partial y}\left(y\Gamma_\phi\frac{\partial V}{\partial y}\right)+\frac{\rho w^2}{y}$	$\frac{1}{Re_c}\sum\frac{1}{L_k}\left(n_k m_k V_k-\frac{4\pi}{3}\rho_k r_k^3 n_k F_{\phi,k}\right)$
Tangential momentum	W	μ_{eff}	$-\left(\frac{\Gamma_\phi}{y}+\rho V+\frac{\partial\Gamma_\phi}{\partial y}\right)\frac{w}{y}$	$\frac{1}{Re_c}\sum\frac{1}{L_k}\left(n_k m_k W_k-\frac{4\pi}{3}\rho_k r_k^3 n_k F_{\phi,k}\right)$
Mass fraction of fuel	Y_{fi}	Γ_{eff}	$-w_{fi}R_{fi}$	$\frac{1}{Re_c}\sum\frac{1}{L_k}\delta_i n_k m_k$
Mass fraction of CO_2	Y_{CO_2}	Γ_{eff}	$\sum\nu_{CO_2,fi}w_{CO_2}R_{fi}$	0
Mass fraction of oxidizer	Y_o	Γ_{eff}	$-\sum\nu_{o,fi}w_o R_{fi}$	0
Energy	h	Γ_{eff}	$(\nu_c-1)M_c^2\frac{DP}{Dt}+\sum w_{fi}Q_i R_{fi}+\rho T\frac{Dc_p}{Dt}$ $-\frac{\partial}{\partial x}\left(\Gamma_\phi T\frac{\partial c_p}{\partial x}\right)-\frac{1}{y}\frac{\partial}{\partial y}\left(y\Gamma_\phi T\frac{\partial c_p}{\partial y}\right)$	$\frac{1}{Re_c}\sum\frac{1}{L_k}n_k m_k\,(h_s-\ell_{k,\text{eff}})$
Turbulent kinetic energy	k	Γ_{eff}	$\mu_t G-\rho\epsilon$	0
Turbulent energy dissipation	ϵ	Γ_{eff}	$C_1C_\mu Gk\rho-C_2\rho\epsilon^2/k$	0
Concentration fluctuation	g_i	Γ_{eff}	$C_{g_1}\mu_{\text{eff}}\left[\left(\frac{\partial Y_{fi}}{\partial x}\right)^2+\left(\frac{\partial Y_{fi}}{\partial y}\right)^2\right]-C_{g_2}\rho g_i\frac{\epsilon}{k}$	0

Turbulent parameters							
C_1	C_2	C_μ	C_{g_1}	C_{g_2}	κ	E	C_R
1.44	1.92	0.09	2.8	2.0	0.4187	9.0	1.0

$$\mu_{\text{eff}}=\frac{\mu_{\ell a}}{Re_c}+\mu_t,\quad \Gamma_{\text{eff}}=\frac{\mu_{\ell a}}{\sigma_{\phi_{\ell a}}Re_c}+\frac{\mu_t}{\sigma_{\phi_t}},\quad \mu_t=C_\mu\rho\frac{k^2}{\epsilon},\quad G=2\left[\left(\frac{\partial U}{\partial x}\right)^2+\left(\frac{\partial V}{\partial y}\right)^2+\left(\frac{V}{y}\right)^2\right]+\left(\frac{\partial w}{\partial x}\right)^2+\left[y\frac{\partial}{\partial y}\left(\frac{w}{y}\right)\right]^2+\left(\frac{\partial U}{\partial y}+\frac{\partial V}{\partial x}\right)^2,\quad F_{\phi,k}=\frac{d\phi_k}{dt}$$

Table 1 contains all of the relevant information pertaining to each of the dependent variables. The gas-phase equations are nondimensionalized, using the inflow conditions of the combustor, which are held fixed in time for the calculations herein. The nondimensionalization gives rise to additional dimensionless groups, namely Re, M_c, and L_k.

The turbulent shear stresses are evaluated using the $(k\text{-}\epsilon)$ model of Launder and Spalding.[10] Use of this turbulence model implies that the influence of droplets on turbulent structure is negligible, and that the possible oscillatory motions have a low frequency which does not appreciably alter the turbulent properties. However, the lower frequency components of turbulent structure can be analyzed directly with the unsteady analysis. The $k\text{-}\epsilon$ model, therefore, might only be employed for the moderate frequency turbulent components. Potential inaccuracies exist in the case of swirling flows for the turbulence model. The extent of these inaccuracies for spray combustors is unknown; furthermore, no clearly better turbulence model has been identified. The combustion model is based on an analogous treatment of turbulent diffusion flames, with the assumption that no envelope flame is present and that the individual droplets act as a source of fuel vapor for the gas phase. The reaction rate is determined by taking into account the minimum of either reaction rates obtained from the eddy break-up model of Spalding[12] or the Arrhenius reaction rate given by Westbrook and Dryer.[16]

$$R_{fi}=\min\left[A\left(\frac{\rho Y_{fi}}{W_{fi}}\right)^a\left(\frac{\rho Y_o}{W_o}\right)^b e^{(-E_{ai}/T)},\ \frac{C_R}{W_{fi}}g_i^{1/2}\left(\frac{\rho\epsilon}{k}\right)\right] \tag{2}$$

Note that in the regions of interest for flame stability studies the chemical kinetics should be slower than molecular mixing within a turbulent eddy. The conversion rate will be given there by the kinetic formula. The use of the eddy break-up model necessitates the solution of additional equations involving g_i.

In the present calculations, a special form of the conservation equation based on energy involving $C_p(T)$ and T is employed. The specific heat of the mixture is given by

$$C_p(T)=\sum_i Y_i C_{p,i}(T) \tag{3}$$

with summation over all species. The chemical kinetics are

modeled by single-step kinetic mechanisms, where each component of the fuel reacts separately with oxidizer to form products. By assuming equal binary diffusion coefficients for all the species and by knowing the mass fractions of the fuel species, CO_2 and oxidizer, and the stoichiometric relationship of the chemical kinetic reaction steps, the mass fractions of the remaining species N_2 and H_2O can be easily determined in terms of simple algebraic expressions. The variation of the specific heats with temperature is considered by using polynomials of the form

$$C_{p,i} = \frac{R}{W_i}(C_{1i} + C_{2i}T + C_{3i}T^2 + C_{4i}T^3 + C_{5i}T^4) \tag{4}$$

The constants in the polynomials are compiled from Refs. 14 and 15. The system of equations for gas phase are completed with the following equation of state:

$$\rho = (\nu_c - 1)\, M_c^2 \frac{P}{RT\sum_i (Y_i/W_i)} \tag{5}$$

In Table 1, σ_ϕ denotes the appropriate value of effective Prandtl or Schmidt number for each ϕ. For all the dependent variables, the values chosen in the present calculations correspond to $\sigma_{\phi_\ell} = 1.0$ and $\sigma_{\phi_t} = 0.9$, with the exception of $\sigma_{\epsilon_t} = 1.217$.

The implementation of the boundary conditions at the solid wall would become straightforward if the grid mesh could be made fine enough to resolve the turbulent boundary-layer structure in the vicinity of the wall. Instead, the source terms in the governing equations of momentum, kinetic energy, dissipation rate, and energy are modified with the introduction of wall functions. The procedure adopted for wall functions is similar to that given in Ref. 11. For the equations involving mass fractions of fuel and oxidizer and concentration fluctuation, the flux normal to the wall is set to zero. Inflow boundary conditions for all dependent variables are prescribed. The radial velocity is set to zero at the axis of symmetry. All other boundary conditions are based on normal gradients which are set to zero at the axis of symmetry and the outflow.

III. Liquid-Phase Equations

Among various advantages of using the Lagrangian formulation for the liquid-phase equations are its ability to handle multivaluedness of solutions in a natural way, elimination of numerical diffusion, and restriction of the Lagrangian calculations to the region where droplets are present so that the Eulerian-Lagrangian approach can be used for very fine resolution where required.[7] The liquid- and gas-phase equations are nondimensionalized with respect to the same scales. However, the droplet radius (r_k') is made dimensionless with respect to its initial radius, ($r_{k,0}'$). Complete description of the liquid-phase equations presented herein can be found in Refs. 7 and 17.

$$\frac{dx_k}{dt} = U_k \tag{6}$$

$$\frac{dy_k}{dt} = V_k \tag{7}$$

$$\frac{dU_k}{dt} = \left(\frac{L_k^2}{Re_c\rho_k}\right)\frac{3}{16}\frac{C_D\mu Re_k}{r_k^2}\,[U_g - U_k] \tag{8}$$

$$\frac{dV_k}{dt} = \left(\frac{L_k^2}{Re_c\rho_k}\right)\frac{3}{16}\frac{C_D\mu Re_k}{r_k^2}\,[V_g - V_k] + \frac{W_k^2}{y_k} \tag{9}$$

$$\frac{dW_k}{dt} = \left(\frac{L_k^2}{Re_c\rho_k}\right)\frac{3}{16}\frac{C_D\mu Re_k}{r_k^2}\,[W_g - W] - \frac{V_k W_k}{y_k} \tag{10}$$

where

$$Re_k = 2\left(\frac{Re_c}{L_k}\right)\frac{r_k\rho_g}{\mu}\,[(U_g - U_k)^2 + (V_g - V_k)^2 + (W_g - W_k)^2]^{1/2} \tag{11}$$

$$C_D = \frac{24}{Re_k}(1 + Re_k^{2/3}/6) \tag{12}$$

Based on the Tong-Sirignano model[8]

$$\frac{dS_k}{dt} = -2\left(\frac{L_k^2}{Re_c\rho_k}\right)\mu\left(\frac{2}{\pi}Re_k\right)^{1/2} f(B_k) \tag{13}$$

The function $f(B_k)$ is obtained from the solution of Emmons' problem.[8] The range of validity of this function is extended in the present calculations to consider the effects of droplet condensation. The following equations are based on the vortex model[8] for the internal droplet temperature and the internal mass fractions of the multicomponent fuel.

$$\frac{\partial T_k}{\partial t} = 17\left(\frac{L_k}{Pe_\ell}\right)\frac{1}{r_k^2}\left\{\eta\frac{\partial^2 T_k}{\partial\eta^2} + [1 + C(t)\,Pr_\ell\eta]\frac{\partial T_k}{\partial\eta}\right\} \tag{14a}$$

and

$$\frac{\partial Y_{ki}}{\partial t} = 17\left(\frac{L_k}{Sc_\ell Re_\ell}\right)\frac{1}{r_k^2}\left\{\eta\frac{\partial^2 Y_{ki}}{\partial\eta^2} + [1 + C(t)\,Sc_\ell\eta]\frac{\partial Y_{ki}}{\partial\eta}\right\} \tag{14b}$$

where

$$C(t) = \frac{3}{17}\left(\frac{Re_\ell}{L_k}\right) r_k\frac{dr_k}{dt} \tag{15}$$

The boundary conditions for Eq. (14) are given by, at $t = t_{\text{injection}}$,

$$T_k = T_{k,0} \tag{16}$$

and

$$Y_{ki} = Y_{ki,0}$$

at $\eta = 0$,

$$\frac{\partial T_k}{\partial\eta} = \frac{1}{17}\left(\frac{Pe_\ell}{L_k}\right) r_k^2\frac{\partial T_k}{\partial t}$$

and

$$\frac{\partial\gamma_{ki}}{\partial\partial\eta} = \frac{1}{17}\left(\frac{Sc_\ell Re_\ell}{L_k}\right) r_k^2\frac{\partial Y_{ki}}{\partial t} \tag{17}$$

at $\eta = 1$,

$$\frac{\partial T_k}{\partial\eta} = \frac{3}{16}\left(\frac{Pr_\ell}{k_\ell}\right)\mu\left(\frac{2}{\pi}Re_k\right)^{1/2}\left[\frac{C_p(T_g - T_{k,s})}{B_k} - \ell_k\right] f(B_k) \tag{18}$$

and

$$\frac{\partial Y_{ki}}{\partial\eta} = \frac{3}{16}\left(\frac{Sc_\ell}{\mu_\ell}\right)\mu\left(\frac{2}{\pi}Re_k\right)^{1/2}[Y_{kis} - \delta_i]\, f(B_k)$$

$$B_k = \frac{C_p(T_g - T_{k,s})}{\ell_{k,\text{eff}}} = \frac{(Y_{fs} - Y_f)}{(1 - Y_{fs})} \tag{19}$$

(Note: The Spalding number is based on Y_{fs} and Y_f in the present calculations.)

$$\ell_{k,\text{eff}} = \ell_k + 4\pi \left(\frac{k_\ell}{Pr_c}\right)\left(\frac{r_k^2}{m_k}\frac{\partial T_k}{\partial r}\right)_s \tag{20}$$

The second term on the right-hand side of the above equation represents the heat transfer to the droplet interior. By knowing the mass fractions of the species in the liquid phase, we may determine the corresponding mole fractions by

$$\chi_{iks} = \frac{Y_{iks}/W_i}{\Sigma Y_{iks}/W_i} \tag{21}$$

At the droplet surface, the mole fractions of the species in the gas phase can be related to the mole fractions of the corresponding species in the liquid phase by means of Raoult's law, in conjunction with the Clasius-Clapeyron relationship.

$$\chi_{is} = \frac{1}{P}\chi_{iks}P_{is} \tag{22}$$

$$P_{is} = \exp\left[\ell c_i\left(\frac{1}{T_{bi}} - \frac{1}{T_{k,s}}\right)\right] \tag{23}$$

The corresponding mass fractions at the droplet surface are given by

$$Y_{is} = \frac{\chi_{is}W_i}{W_a(1-\Sigma\chi_{is}) + \Sigma W_i\chi_{is}} \tag{24}$$

The fractional mass vaporization rate of fuel species i is given by

$$\delta_i = Y_{is} + (1 - Y_{fs})\frac{Y_{is} - Y_{fi}}{Y_{fs} - Y_f} \tag{25}$$

where

$$Y_{fs} = \sum Y_{is} \tag{26}$$

$$Y_f = \sum Y_{if} \tag{27}$$

The latent heat of vaporization is given by

$$\ell_k = \sum \delta_i \ell_{ki} \tag{28}$$

In Eq. (11) the molecular viscosity is evaluated at a reference temperature using Sutherland's equation

$$\mu(T_{ref}) = \mu_c\left(\frac{T_{ref}}{T_c}\right)^{3/2}\frac{T_c + b_1}{T_{ref} + b_1} \tag{29}$$

where

$$T_{ref} = \frac{1}{3}T_g + \frac{2}{3}T_{k,s} \tag{30}$$

The Tong-Sirignano model is based on the boundary-layer approximation for the gas phase and is applicable for high-droplet Reynolds numbers. The model predicts low vaporization rates at low Reynolds numbers because of $Re_k^{1/2}$ dependence and is valid only for Reynolds number higher than 0(10). It is, therefore, appropriate to switch from the Tong-Sirignano model to some valid low Reynolds number model as the droplet Reynolds number becomes small. The vaporization model used for low Reynolds numbers has the correction for convective effects considered through the empirical correlations obtained from Ref. 9. The switching between the vaporization models is accomplished by replacing the term $2[(2/\pi)Re_k]^{1/2}\ f(B_k)$ of Eqs. (13) and (18) with the following expressions:

$$[1 + (1 + Re_k)^{1/3}]\ Re_k^{0.077}\ \ell n(1 + B_k)$$

where $1 < Re_k < 20$ or

$$[1 + (1 + Re_k)^{1/3}]\ \ell n(1 + B_k)$$

when $Re_k \leq 1$. The implication of switching between vaporization models needs further investigation.

The droplets may evaporate, shatter, and/or reflect with reduced momentum upon droplet impingement with combustor walls. In the absence of detailed experimental verification, it is assumed that the droplets undergo instantaneous vaporization upon droplet collision with the walls.

IV. Solution Procedure

The governing equations of the gas phase are solved via the TEACH computational algorithm of Patankar and Spalding.[18] The liquid-phase equations for the position, velocity, and vaporization rate of the particles are advanced in time by the second-order accurate explicit Runge-Kutta method. The partial differential equations governing the internal distributions of the droplet temperature and the mass fractions are integrated by a fully implicit numerical method.

A second-order accurate linear interpolation scheme is used for evaluating the gas-phase properties at the characteristic location and also for redistributing the liquid-phase source term contributions (of the gas-phase equations evaluated at the characteristic location) amongst the surrounding Eulerian nodes. The numerical method employed for the gas-phase equations allows for the integration to be performed over a larger time step, whereas the allowable time step for the liquid-phase equations is found to be much smaller than the convective time-scale resolved over the smallest of the nonuniform mesh sizes. To improve the overall efficiency of the computational procedure, a fractional time-step method is developed which allows for the integration between the gas and liquid phases to be performed with different time steps. The details of the solution procedure and also of various aspects associated with the injection of the particles, such as the injection time interval and the number of droplets contained in each of the characteristic droplet groups (n_k), can be found in Raju and Sirignano.[3] The solution procedure based on the unsteady equations has been used in the present computations to obtain the steady-state solution.

V. Parameter and Configuration Selections

The numerical procedure is applied to predict the flow properties of the ducted, axisymmetric bluff-body configuration of Fig. 1.[14] The mixing characteristics of the flowfield are influenced by the interaction between the bluff-body wake and the injected fuel spray emanating from a swirl-atomizer located in the middle of the centerbody face. The primary air stream originates from a swirler located in the bluff-body flame holder, and the dilution stream passes through the annulus between the bluff body and the cylindrical duct. However, most of the calculations in the present study have been performed under simplified flow conditions, where the interaction between the primary air stream and the injected fuel

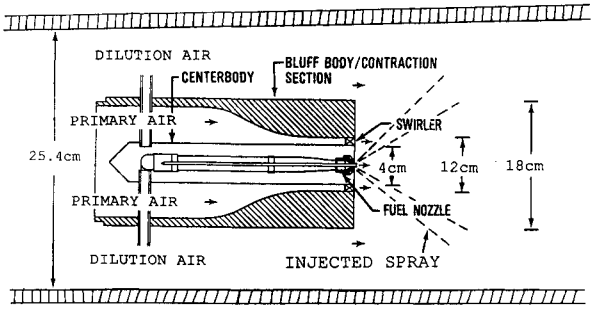

Fig. 1 Geometry of the flow configuration.

Table 2 Inflow conditions for different cases examined

Case	1	2	3	4	5	6	7	8
Primary air								
Axial velocity, m/s	20	20	20	20	20	20	20	20
Swirl velocity, m/s	20	30	20	20	20	20	20	20
Swirl number	0.722	1.08	0.722	0.722	0.722	0.722	0.722	0.722
Mass flow rate, kg/s	0.272	0.272	0.272	0.272	0.272	0.272	0.272	0.272
Dilution air								
Axial velocity, m/s	——	——	18.54	——	——	——	——	——
Mass flow rate, kg/s	——	——	0.635	——	——	——	——	——
Liquid spray								
Mass fraction of *n*-decane	0.3	0.3	0.3	0.0	0.3	1.0	0.3	1.0
Mass fraction of *n*-octane	0.3	0.3	0.3	0.0	0.3	0.0	0.3	0.0
Mass fraction of *n*-hexane	0.4	0.4	0.4	1.0	0.4	0.0	0.4	0.0
Mass flow rate, kg/s	0.016	0.016	0.016	0.016	0.0049	0.0049	0.0029	0.0029
Equivalence ratio, Φ	1.0	1.0	0.3	1.0	0.3	0.3	0.18	0.18

spray alone is examined. The values used in the computation for the inflow conditions of various cases examined are summarized in Table 2.

The inflow conditions for cases 1-4 are chosen such that the primary air/fuel mass flow rates correspond to an equivalence ratio of unity. However, the equivalence ratio based upon the actual amounts of air/fuel mass flow rates participating in the primary reaction zone is found to be fuel-rich under the inflow conditions of cases 1-4. The calculations for cases 5-8 are performed to evaluate the effect of fuel composition under the inflow conditions of reduced mass flow rates, where the fuel composition in the primary reaction zone varies from near-stoichiometric to near-weak-extinction conditions.

The other relevant gas-phase inflow conditions are given by $T_c' = 500$ K, $p_c' = 2$ atm, $\rho_c' = 1.359$ Kg/m^3, $k_c' = 0.03\ (U_c')^2$, and $\epsilon_c' = k_c'^{1.5} C_\mu^{0.75}/0.0009$. The temperature of the isothermal walls, cylindrical duct, and bluff-body surfaces is taken to be 750 K. The injected spray is assumed to comprise four conical streams and the half-angles of the corresponding streams are given by $\theta = 5$, 10, 15, and 20 deg. The polydisperse character of the spray is taken into account by discretizing each of the conical streams by four droplet groups, based on initial droplet radii of $r_{k,0} = 75$, 60, 45, and 30 μm. The mass flow rates contained amongst each of the droplet groups are assumed to be equal. The initial conditions for the droplets are given by $T_{k,0} = 300$ K, $V_{k,0}' = 1.3$-5.13 m/s, $U_{k,0}' = 14.94$-14.09 m/s, and $W_{k,0}' = 7.5$ m/s. The gas-phase equations are solved on a grid with a mesh size of 36 axial nodes × 34 radial nodes. An exponential stretching is used in the axial direction to yield a denser grid near the combustor inlet. For each of the cases examined, about three hours of CPU time on a VAX 780 are required for the calculations to reach a steady state using the following time steps:

$$\Delta t'_{\text{injection}} = 1.0 \text{ ms}, \quad \Delta t_g' = 1.0 \text{ ms}, \text{ and } \Delta t_\ell' = 0.004 \text{ ms}$$

VI. Results and Discussion

The global features of the flow structure can be ascertained from Figs. 2a-2d showing, respectively, the velocity vector plot, the isotherms, the contours of the combined mass fractions of *n*-decane, *n*-octane, and *n*-hexane, and also of the mass fraction of oxygen for case 1. The figures have an elongated scale in the radial direction. The near wake of this flow configuration is essentially characterized by two vortices. The swirl-induced primary vortex, oriented in the clockwise direction, is centered at axial and radial coordinates of 0.1 and 0.042 m, respectively. The maximum reversed flow rate, which

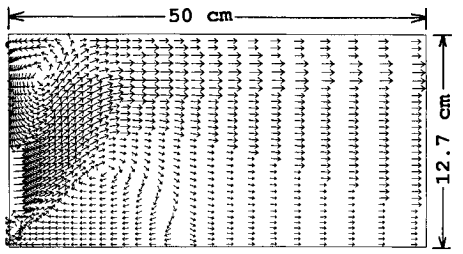

Fig. 2a Velocity vector plot for case 1.

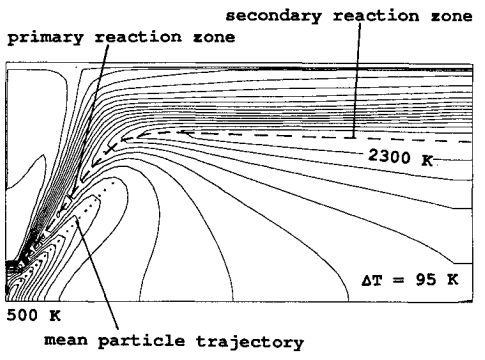

Fig. 2b Temperature contours for case 1.

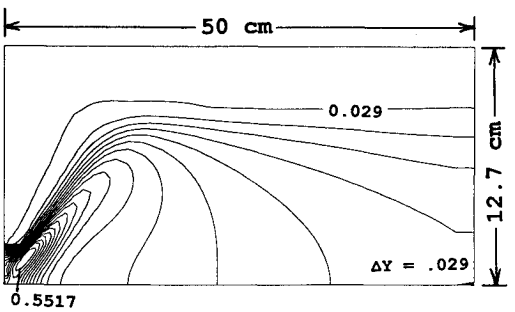

Fig. 2c Contours of fuel mass fraction for case 1.

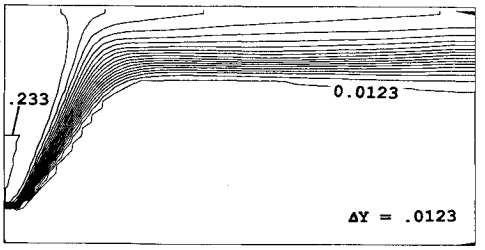

Fig. 2d Contours of oxidizer mass fraction for case 1.

characterizes the strength of the vortex, is found to be 4.3% of the primary air mass flow rate. The mixing and combustion characteristics of the flowfield are not affected directly by the presence of the outer vortex, which is oriented in the counterclockwise direction, as it is mostly the primary air that recirculates essentially within a uniform temperature region. In Fig. 2b, the dashed line identifies the location of the fast reaction zone. An examination of the velocity plot and temperature contours reveals that the swirl-induced primary reaction zone is located to the left of the zero mean axial velocity contour of the inner vortex. In the primary reaction zone, the fuel vapor from the vaporizing droplets mixes with the incoming air and the combustion products entrained in the recirculation act as a continuous source of ignition. The dotted line in Fig. 2b indicates the mean path of the droplet trajectories. The cooling effect associated with the droplet evaporation can be evidenced from the temperature distribution in this region. As primary air moves radially outwards, because of swirl, between the regions of recirculation, part of the oxygen mass reacts with fuel to form products in the primary reaction zone, and the remainder moves downstream through the outer region. The unburnt fuel, together with the combustion products, moves downstream of the primary vortex through the inner region. Further downstream of the primary reaction zone, combustion proceeds in the secondary reaction region, as mixing between the oxidizer and the reactants occurs within the shear layer. The temperature attains a maximum value of 2300 K in the secondary reaction zone. The mass fraction contour lines of the reactants and the oxidizer shown in Figs. 2c–2d, respectively, identify the fuel- and oxidizer-rich regions of the combustor. The results show that the region of maximum concentration is located close to the fuel injector.

The droplet trajectories are shown in Fig. 3. The polydisperse character of the spray is represented by different symbols, which indicate the initial sizes of the droplet groups. Initially, the droplets are clustered together and move linearly about a mean conical half-angle of 33 deg before they become small enough to be deflected by the gaseous flow. The initial droplet Reynolds numbers range between $25 \leq Re_{k,0} \leq 80$. It takes about 20 ms for the complete vaporization of the droplets, and vaporization is completed at about 0.284 m along the combustion chamber. Figure 4 shows the time variation of the normalized droplet radius squared for different droplet groups of the stream, $\theta = 5$ deg. It takes 4 ms for the smallest droplets to evaporate and about 18 ms for the largest size droplets. The initial slope of these curves is small, as most of the heat flux from the gas phase goes into the heating of the droplet so that less thermal energy is available for vaporization. After the initial period, the time variation of the droplet radius squared becomes more linear, as the droplet temperature approaches close to the wet-bulb temperature and more of the heat that is available from the gas phase goes into the vaporization of the droplet. Figure 5 shows the time variation of the mass fractions of the fuel species at the droplet surface and of the Reynolds number for the droplet group, $\theta = 5$ deg and $r'_{k,0} = 75$ μm. The Reynolds number increases slightly initially, owing to an increase in the density resulting from the low-temperature and fuel-rich conditions of the gas phase near the fuel injector. The Reynolds number falls below 10 after 6 ms, and more than 60% of the droplet mass has vaporized during this time period. Since n-hexane is the most volatile component of the liquid spray, it vaporizes rapidly in the initial phase. However, owing to the large diffusional resistance associated with the high Lewis number (= 10), the mass fraction of hexane at the surface does not reach a zero value but asymptotes at a low positive value. The mass fraction of n-octane rises initially and then decreases until it asymptotes at a value higher than the corresponding level of n-hexane during the later part of the droplet lifetime. The liquid-phase diffusion remains important during the entire droplet lifetime. Similarly, droplet heating is also found to remain important during most of the droplet lifetime.

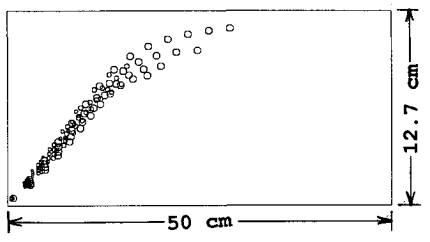

Fig. 3 Droplet trajectories for case 1.

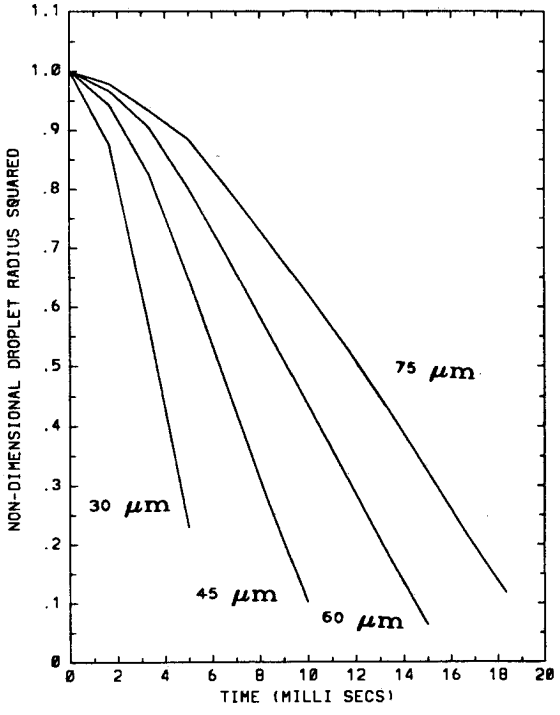

Fig. 4 S_k vs t' for droplets of the stream, $\theta = 5$ deg of case 1.

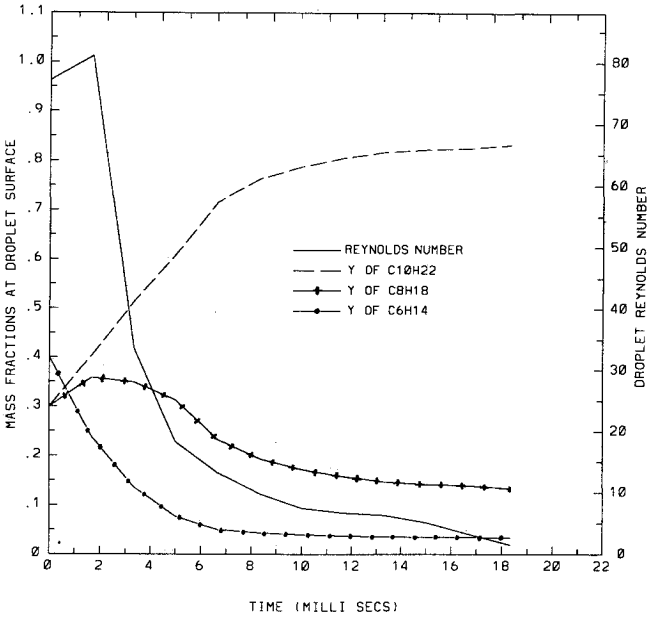

Fig. 5 Y_{iks} and R_k vs t' for one droplet group of case 1.

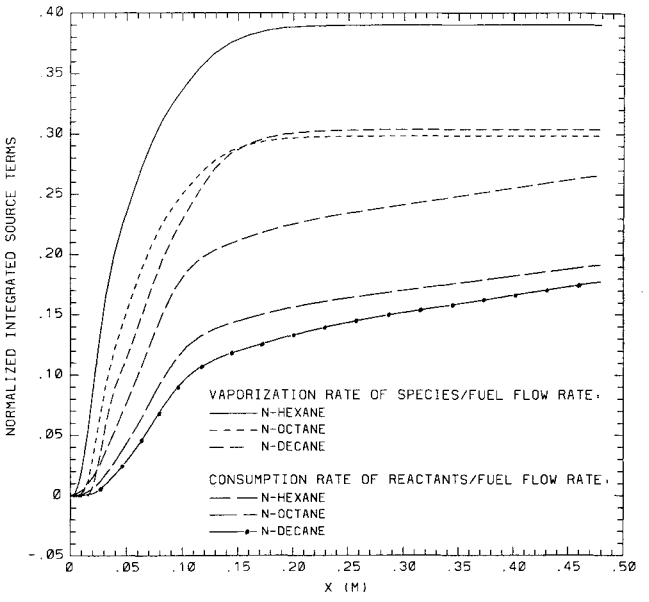

Fig. 6 Axial variation of multicomponent fuel evaporation and consumption rates for case 1.

The distribution of the normalized mass fractions of evaporated fuel and of the consumed fuel along the combustion chamber are shown in Fig. 6. The results shown are obtained by integrating the source term contributions of the gas-phase equations arising from the production of fuel species due to vaporization. Also shown is the accumulated consumption of reactants due to combustion in the gas phase along the combustion chamber. The slopes of the curves indicate that the vaporization rates and species conversion rates depend strongly upon fuel volatility. The results indicate very slight condensation of the heavier components near the droplet injector location. When the vaporization is complete, the normalized mass fractions of the evaporated species approach their respective initial liquid-phase values. The consumption rate of the fuel species is largest in the primary reaction zone. Further downstream of the primary reaction zone, the reduced reaction rates reflect the mixing rate behavior of the turbulent shear layers. The variation of the consumption rate of fuel species becomes nearly linear in the axial direction during the final stage of the combustion process. The surface plot of the normalized reaction rate is shown in Fig. 7. The grid shown in the figure corresponds with the numerical grid of the computational domain. The results show that the reaction originates in the inner region of the primary air stream as it enters the combustion chamber. The flame spreads in the primary reaction zone. The Arrhenius kinetics are found to be rate-controlling in the outer regions of the primary reaction zone, where the temperatures are low. In the inner region of the primary reaction zone and also in the secondary reaction zone, where the temperatures are large, the eddy break-up term is found to be rate controlling. More than 80% of the total amount of fuel consumed during the combustion process occurs under the conditions where the mixing rate is rate controlling.

The overall efficiency of the combustor for cases 1-4 can be seen in Fig. 8, where the integrated vaporization and consumption rates of the fuel along the combustion chamber are plotted. The vaporization and consumption rates are normalized with respect to the initial fuel flow rate. The improvements in the rates of evaporation and consumption, due to an increase in the swirl number, can be noted from the comparisons of cases 1 and 2. The effect of adding a separate dilution stream of zero swirl can be examined from the comparison of cases 1 and 3. The effect of fuel composition can be seen from the comparison of cases 1 and 4. The fuel in case 4 is pure

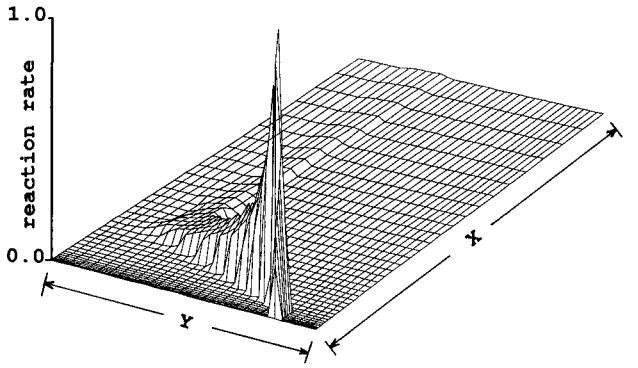

Fig. 7 Surface plot of the normalized reaction rate for case 1.

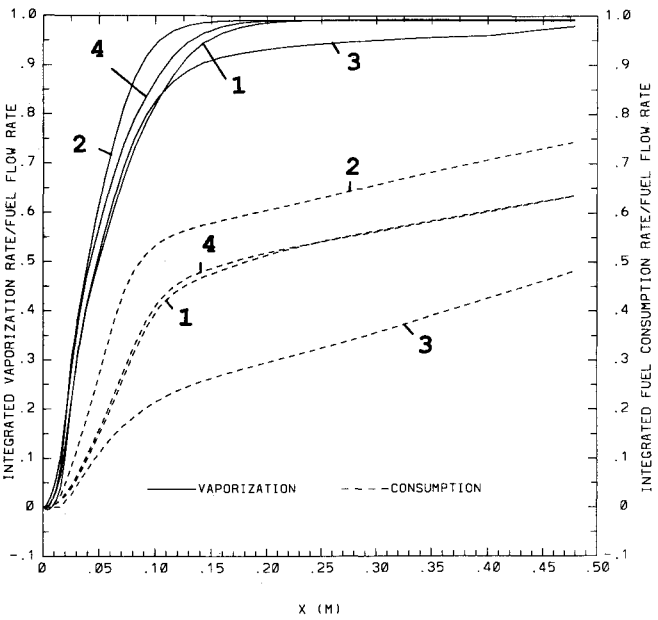

Fig. 8 Axial variation of fuel evaporation and consumption rates for cases 1-4.

n-hexane, as compared to the multicomponent liquid spray of case 1. The rate of evaporation is slightly faster in case 4, as *n*-hexane is the most volatile of three components considered in case 1. In cases 1, 2, and 4, it is seen from Fig. 8 that the time for vaporization of the first 40–50% of fuel is one-third to one-half the time for energy conversion. This indicates that droplet vaporization rate is a controlling factor, together with mixing, in the early combustion stage. For the final 50–60% of the conversion, the conversion time is much larger than the vaporization rate, so that mixing is clearly the major factor in the final stages of combustion. The differences in the conversion rates during the early stages of combustion due to the variation in fuel composition are found to be small, since the eddy break-up term is rate controlling during most of the combustion process and heats of combustion of the three fuel species have nearly identical values.

The axial variation of the integrated vaporization and consumption rates for cases 5–8 are shown in Fig. 9. The effects of reduced fuel mass flow rates and of different fuel composition can be examined from the comparison of cases 5–8. The fuel in cases 5 and 7 comprises *n*-decane, *n*-octane, and *n*-hexane components and in cases 6 and 8 is pure *n*-decane. Reduction in the fuel mass flow rate for cases 5 and 6 is such that the equivalence ratio based on the initial fuel/air mass flow rates has a value of 0.3, whereas for cases 7 and 8 its value is reduced further, down to 0.18 near the weak-extinction limit. In cases 5 and 6, most of the combustion process is completed

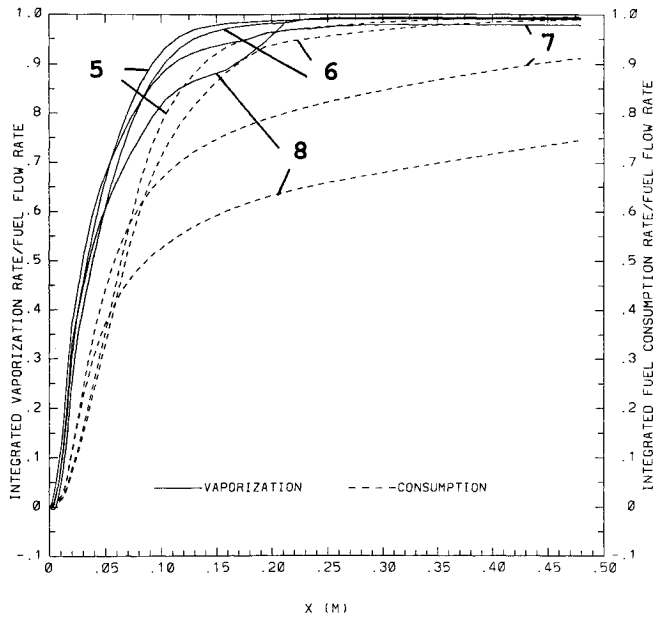

Fig. 9 Axial variation of fuel evaporation and consumption rates for cases 5–8.

within the primary reaction zone, and the highest temperatures are also observed to occur within the primary reaction zone. Comparison of the results between cases 5 and 6 shows that the effect of reduced volatility results in a reduction of both evaporation and reaction rates. By a further reduction in the fuel flow rate, the differences in the evaporation and reaction rates become more significant, as can be seen from the comparison of cases 7 and 8. In these cases, the evaporation rate in the initial period is larger, as the droplets are observed to pass through the high-temperature region of the flame located close to the atomizer. Further vaporization takes place in a relatively low-temperature region, as the droplets move away from the primary reaction zone. The increased vaporization rate in the region between $x = 0.15$ to 0.2 m of case 8 is due to droplet impingement on the combustor walls.

Comparison of Figs. 8 and 9 indicates that the vaporization rate does not vary much as the equivalence ratio is reduced. Both mixing and conversion rates tend to approach vaporization rates as the equivalence ratio goes to 0.3. As the equivalence ratio is further decreased, chemical reaction rates become smaller, so that the difference between vaporization rates and conversion rates becomes larger.

VII. Concluding Remarks

The results demonstrate that droplet vaporization, turbulent mixing, and energy conversion play an important role in various aspects of the combustor performance. Although the predictions remain to be validated with experimental results, the internal consistency exhibited by the predictions supports the belief that agreement will be close to the actual flow behavior. The anticipated success should be restricted to the mean flow behavior. If the previous studies[13,14] are any indication, the predictions of the rms fields will be poor for the application of the k-ϵ turbulence model. The turbulence model could be improved by incorporating the algebraic stress model, which has been shown to yield better results for swirl flows.[19] Although the eddy break-up model of Spalding has been used extensively in the modeling of turbulent gaseous flames, its application for spray combustion requires experimental validation. The accuracy of the vaporization model could also be improved by considering the effects associated with physical property variations. The effect of fuel composition is found to be significant near the weak-extinction limits, but its effects near the blow-off conditions remains to be explored.

References

[1]El Banhawy, Y. and Whitelaw, J. H., "Calculation of the Flow Properties of a Confined Kerosene-Spray Flame," *AIAA Journal*, Vol. 18, No. 12, 1980, pp. 1503–1510.

[2]Swithenbank, J., Turan, A., and Felton, P. G., "Three-Dimensional Two-Phase Mathematical Modelling of Gas Turbine Combustors," *Gas Turbine Combustor Design Problems*, Hemisphere, Washington, D.C., 1980, pp. 249–314.

[3]Raju, M. S. and Sirignano, W. A., "Spray Computations in a Centerbody Combustor," *Proceedings of the 1987 ASME/ISME Thermal Engineering Joint Conference*, ASME, Vol. 1, 1987, pp. 61–71.

[4]Lefebvre, A. H., *Gas Turbine Combustion*, Hemisphere, Washington, D.C., 1983.

[5]Kramlich, J. C., Heap, M. P., Seeker, W. R., and Samuelsen, G. S., "Flame-Mode Destruction of Hazardous Waste Compounds," *20th Symposium (International) on Combustion*, The Combustion Institute, Pittsburgh, PA, 1984, pp. 1991–1999.

[6]Oechsle, V. L., Ross, P. T., and Mongia, H. C., "High Density Fuel Effects on Gas Turbine Engines," AIAA Paper 87-1829, Sept. 1987.

[7]Sirignano, W. A., "Fuel Droplet Vaporization and Spray Combustion," *Progress in Energy and Combustion Science*, Vol. 9, No. 4, 1983, pp. 291–322.

[8]Tong, A. Y. and Sirignano, W. A., "Multicomponent Transient Droplet Vaporization with Internal Circulation: Integral Formulation and Approximate Solution," *Numerical Heat Transfer*, Vol. 10, No. 3, 1986, pp. 253–278.

[9]Clift, R., Grace, J. R., and Weber, M. E., *Bubbles, Drops, and Particles*, Academic, New York, 1978.

[10]Launder, B. E. and Spalding, D. B., *Mathematical Models of Turbulence*, Academic, London, England, 1972.

[11]Khalil, E. E., Spalding, D. B., and Whitelaw, J. H., "The Calculation of Local Flow Properties in Two-Dimensional Furnaces," *International Journal of Heat and Mass Transfer*, Vol. 18, No. 6, 1975, pp. 775–791.

[12]Spalding, D. B., "Mathematical Models of Turbulent Flames: A Review," *Combustion Science and Technology*, Vol. 13, Nos. 1–6, 1976, pp. 3–25.

[13]Raju, M. S. and Krishnamurthy, L., "Computational Fluid Dynamic Studies of Certain Ducted Bluff-Body Flowfields Relevant to Turbojet Combustors. Vol. I: Time-Dependent Calculations with the k-ϵ Turbulence Model for an Existing Centerbody Combustor," Air Force Wright Aeronautical Lab., Dayton, OH, AFWAL-TR-86-2004, July 1986.

[14]Raju, M. S. and Krishnamurthy, L., "Computational Fluid Dynamic Studies of Certain Ducted Bluff-Body Flowfields Relevant to Turbojet Combustors. Vol. I: Time-Averaged Flowfield Predictions for a Proposed Centerbody Combustor," Air Force Wright Aeronautical Lab., Dayton, OH, AFWAL-TR-86-2004, July 1986.

[15]*CRC Handbook of Physics and Chemistry*, Chemical Rubber Co., Cincinnati, OH, 1978.

[16]Westbrook, C. K. and Dryer, F. L., "Chemical Kinetic Modeling of Hydrocarbon Combustion," *Progress in Energy and Combustion Science*, Vol. 10, No. 1, 1984, pp. 1–57.

[17]Aggarwal, S. K., "Modeling of Multicomponent Fuel Spray Vaporization," *International Journal of Heat and Mass Transfer*, Vol. 30, 1987, No. 9, pp. 1949–1961.

[18]Patankar, S. V., *Numerical Heat Transfer and Fluid Flow*, Hemisphere, Washington, D.C., 1980.

[19]Gupta, A. K., Lilley, D. G., and Syred, N., *Swirl Flows*, Energy and Engineering Science Series, Abacus, Kent, England, 1984.